



Sign-tunable anomalous Hall effect induced by two-dimensional symmetry-protected nodal structures in ferromagnetic perovskite thin films

Byungmin Sohn^{1,2,7}, Eunwoo Lee^{1,2,3,7}, Se Young Park⁴✉, Wonshik Kyung^{1,2}, Jinwoong Hwang⁵, Jonathan D. Denlinger⁵, Minsoo Kim^{1,2}, Donghan Kim^{1,2}, Bongju Kim^{1,2}, Hanyoung Ryu^{1,2}, Soonsang Huh^{1,2}, Ji Seop Oh^{1,2}, Jong Keun Jung^{1,2}, Dongjin Oh^{1,2}, Younsik Kim^{1,2}, Moonsup Han⁶, Tae Won Noh^{1,2}, Bohm-Jung Yang^{1,2,3}✉ and Changyoung Kim^{1,2}✉

Magnetism and spin-orbit coupling are two quintessential ingredients underlying topological transport phenomena in itinerant ferromagnets. When spin-polarized bands support nodal points/lines with band degeneracy that can be lifted by spin-orbit coupling, the nodal structures become a source of Berry curvature, leading to a large anomalous Hall effect. However, two-dimensional systems can possess stable nodal structures only when proper crystalline symmetry exists. Here we show that two-dimensional spin-polarized band structures of perovskite oxides generally support symmetry-protected nodal lines and points that govern both the sign and the magnitude of the anomalous Hall effect. To demonstrate this, we performed angle-resolved photoemission studies of ultrathin films of SrRuO₃, a representative metallic ferromagnet with spin-orbit coupling. We show that the sign-changing anomalous Hall effect upon variation in the film thickness, magnetization and chemical potential can be well explained by theoretical models. Our work may facilitate new switchable devices based on ferromagnetic ultrathin films.

The interplay between magnetism and spin-orbit coupling (SOC) underlies the various topological transport phenomena seen in metallic ferromagnets^{1–3}. In three-dimensional (3D) ferromagnets, spin-polarized bands often accompany nodal points or nodal lines (NLs)^{4–6}. The lifting of the band degeneracy at a nodal structure due to SOC induces enhanced Berry curvature around it, which leads to various topological transport phenomena such as the anomalous Hall effect (AHE)^{7–9}. For instance, in the SrRuO₃ (SRO) bulk, theoretical predictions have indicated that nodal structures with an SOC-induced gap play a role as magnetic monopoles in momentum space, which leads to a non-monotonous change in the AHE¹⁰.

The 3D SRO bulk has been considered as a canonical system, in which the topological band structure induces a large AHE^{10,11}. However, the existence of magnetic monopoles in SRO has not yet been verified experimentally. Part of the reason for this is the lack of a suitable single crystal, as well as the difficulty in preparing clean, cleaved surfaces for angle-resolved photoemission spectroscopy (ARPES) study, due to its 3D structure. Meanwhile, it has recently been shown that the NLs of 3D spin-polarized bands can also induce a large AHE, as seen in a layered Fe₃GeTe₂ ferromagnet⁶. The AHE driven by nodal points (so-called Weyl points) has also been reported in various 3D magnetic metals^{12,13}.

The relationship between the topological band structure and corresponding transport phenomena remains largely unexplored in two-dimensional (2D) metallic ferromagnets³. The nodal structures in 2D ferromagnets are more fragile and unstable compared

with 3D structures. Only when proper symmetry conditions are satisfied can nodal points or NLs manifest as symmetry-protected band degeneracy in 2D bands^{14,15}. Moreover, the increased correlations expected in the reduced dimensionality could alter both the quasi-particle energy spectrum and intrinsic AHE such that careful comparison between theoretical and experimental results is indispensable to verify the topological band structure in 2D magnets^{16,17}.

In this work, we demonstrate the relation between the symmetry-protected nodal structures of 2D spin-polarized bands and the AHE. For this purpose, we performed ARPES measurements on SRO ultrathin films, revealing their band structures. Based on tight-binding models, first-principles calculations and symmetry analysis, we propose that the spin-polarized bands derived from *t*_{2g} orbitals in layered perovskite oxides generally support (1) nodal points with quadratic band crossing (QBC) protected by four-fold rotation symmetry and (2) NLs arising from the crossing between majority and minority spin bands. When SOC is included, these nodal points and NLs are gapped and generate a large Berry curvature in the surrounding area. Because the energies of nodal points and NLs are different, when the Berry curvatures that arise from them have opposite signs, the magnitude and sign of the AHE can generally be varied by changing the Fermi level. We demonstrate that the AHE of SRO thin films exhibits sign reversal, depending on the film thickness, temperature, magnetization and chemical potential, due to the symmetry-protected nodal structures of the 2D spin-polarized bands.

¹Center for Correlated Electron Systems, Institute for Basic Science, Seoul, Korea. ²Department of Physics and Astronomy, Seoul National University, Seoul, Korea. ³Center for Theoretical Physics, Seoul National University, Seoul, Korea. ⁴Department of Physics and Origin of Matter and Evolution of Galaxies (OMEG) Institute, Soongsil University, Seoul, Korea. ⁵Advanced Light Source, Lawrence Berkeley National Laboratory, Berkeley, CA, USA. ⁶Department of Physics, University of Seoul, Seoul, Korea. ⁷These authors contributed equally: Byungmin Sohn, Eunwoo Lee. ✉e-mail: sp2829@ssu.ac.kr; bjyang@snu.ac.kr; changyoung@snu.ac.kr

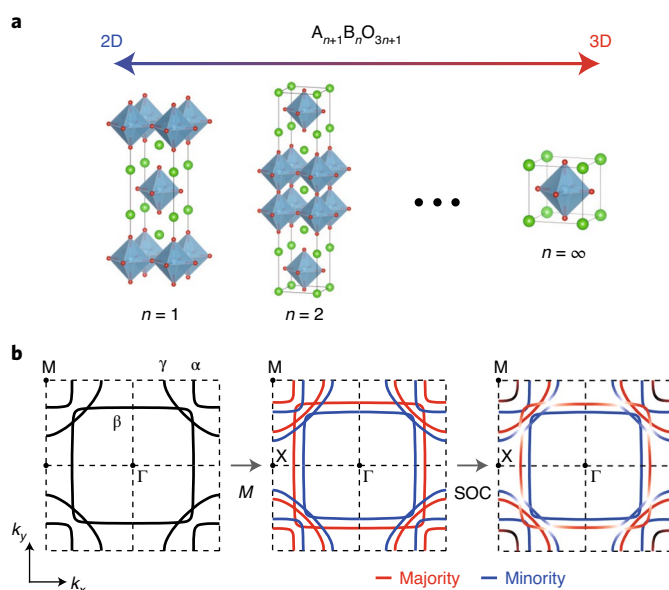


Fig. 1 | FS of 2D ferromagnetic perovskites. **a**, Structures of layered perovskite oxides with the chemical formula $A_{n+1}B_nO_{3n+1}$ where $n=1, 2, \dots$ denotes a natural number. As n increases, the electronic structure changes from 2D to 3D. Green, grey and red atoms represent A, B and O, respectively. **b**, Schematic FSs of SRO in the 2D limit, consisting of three bands (α , β and γ). When magnetization (M) and SOC are absent, all bands are spin degenerate. When M is finite, spin degeneracy is lifted, such that majority (red) and minority (blue) bands form. On initiating SOC, the FSs become hybridized, inducing a finite Berry curvature.

Figure 1a shows the general lattice structures of layered Ruddlesden–Popper perovskite oxides, with the chemical formula $A_{n+1}B_nO_{3n+1}$, where n denotes a natural number. As n increases, the material takes on a more 3D character, interpolating between the 2D limit with $n=1$ (A_2BO_4) and the 3D limit with $n=\infty$ (ABO_3). Among the perovskite materials, SRO is a representative example of 3D ferromagnetic metals, with an AHE that has been attributed to the magnetic monopoles in momentum space of the topological band structure¹⁰.

As the 2D Sr_2RuO_4 is non-magnetic¹⁸, it is not an appropriate system for our study. Therefore, as an alternative, we studied the quasi-2D limit of SRO by growing ultrathin films of SRO with a thickness of four unit cells (u.c.). Due to its quasi-2D nature, the Fermi surfaces (FSs) of SRO ultrathin films are expected to be somewhat similar to those of Sr_2RuO_4 (ref. 19). We confirm this through our ARPES measurements, as will be shown later. For Sr_2RuO_4 , it is well known that the FSs consist of three bands, α , β and γ , where α and β FSs are composed of $d_{xz,yz}$ orbitals, while the γ FS arises from the d_{xy} orbital, as schematically shown in Fig. 1b (refs. 19,20). When ferromagnetism develops, spin-degenerate bands split into majority and minority bands, which results in six bands derived from t_{2g} orbitals appearing at the Fermi level. With SOC, the majority and minority bands are hybridized at the points where they are crossed. This provides the general idea on how Berry curvature is generated in ferromagnetic 2D perovskites.

ARPES results

To experimentally verify the band structure of a 2D ferromagnetic perovskite, we performed ARPES measurements on SRO ultrathin films. Figure 2a shows a FS map as well as the energy–momentum (E – k) spectra of a 4 u.c. SRO thin film measured with 80 eV light with linear horizontal (LH) polarization. The α and β FSs are clearly visible and are similar to the corresponding FSs reported for

Sr_2RuO_4 (refs. 19–22). Due to the rotational distortion of RuO_6 octahedra in SRO ultrathin films grown on $SrTiO_3$ (001) substrates^{23,24}, the FS from the folded β band (β') is also observed.

Whether ultrathin films indeed possess 2D electronic structures requires an examination of the k_z (that is, photon energy) dependence. The measured k_z dispersion is shown in Fig. 2b. Here k_z is calculated based on an inner potential of 14 eV obtained from experiments on SRO single crystals (Oh, J. S. et al., manuscript in preparation). Unlike 3D materials exhibiting k_z dispersion, the β band does not show any k_z dispersion as expected. This clearly illustrates that SRO ultrathin films have quasi-2D band structures, similar to Sr_2RuO_4 (refs. 20,22) and $Sr_3Ru_2O_7$ (ref. 25).

In Fig. 2c, we reproduce the measured FSs. In addition to the α and β pockets shown by the dotted lines, there are more detailed structures. Superimposed on the map as thick lines are results obtained from an effective 2D tight-binding model fit (Methods for details). It is seen that the effective 2D model can explain the major features of the experimental dispersions. We also performed circular dichroism ARPES (CD-ARPES) to examine the Berry curvature, and the result is shown in the bottom-right corner of the figure (Supplementary Information for analysis of the CD-ARPES data). Moving from Γ to M, the intensity of CD data varies from zero to negative, and then to positive. A clear sign-changing behaviour is observed as a function of the electron momentum. Detailed discussions on the tight-binding fit and CD-ARPES results will be discussed later with Fig. 5.

Since ARPES measurement is sensitive to the surface condition, clearer band features can be resolved via in situ measurements. Figure 2d shows a FS map of the 4 u.c. SRO thin film in situ measured with linear vertical (LV) polarized He-I α light (21.2 eV). Spin polarization of the bands was also obtained by performing spin-resolved ARPES (SARPES) measurements below and above the Curie temperature, $T_C \approx 110$ K. Figure 2e shows the spin-resolved energy distribution curves and spin polarizations at the M point at 10 K (below T_C) and 125 K (above T_C). The energy distribution curves below T_C show a considerable difference between the majority and minority spins, whereas no difference was observed above T_C . The difference is also presented in the form of spin polarization, $P = (I_{\uparrow} - I_{\downarrow}) / (I_{\uparrow} + I_{\downarrow})$, where I_{\uparrow} (I_{\downarrow}) is the intensity of the majority (minority) spin measured with SARPES, in the lower panels. Spin-resolved energy distribution curves along the high-symmetry lines (Γ –M and Γ –X) can be found in the Supplementary Information. These observations are consistent with itinerant ferromagnetism^{26,27}.

The high-resolution FS map in Fig. 2d shows more detailed features in comparison with the result from ex situ films in Fig. 2a. An important feature visible in the high-resolution data is heavy bands observed at the Γ and M points. To investigate those heavy bands, the Γ –M cut of the data in Fig. 2d and its momentum distribution curve at the Fermi level are shown in Fig. 2f. To see the dispersion more clearly, we plot the 2D curvature²⁸ of the data near the M point in the inset. Two hole-like bands are observed at the M point: one from the α band and the other, unknown and labelled as A, located within the α pocket. The latter does not exist in the case of Sr_2RuO_4 . We fitted the momentum distribution curve with Lorentzian peaks as shown in the upper panel of Fig. 2f. Near the M point, three peaks are observed: two from the α band and one from the A band. We also find that the heavy bands near the Γ point are α and A replica bands due to the $\sqrt{2} \times \sqrt{2}$ rotational distortion of RuO_6 octahedra^{23,24} (Supplementary Information for low-energy electron diffraction patterns).

Transport and magnetic properties

With the full experimental electronic structure identified, we turn our attention to the transport and magnetic properties of SRO ultrathin films, presented in Fig. 3. Figure 3a shows the thickness-dependent Hall resistivity measured at 10 K for 3.8–5.0 u.c.

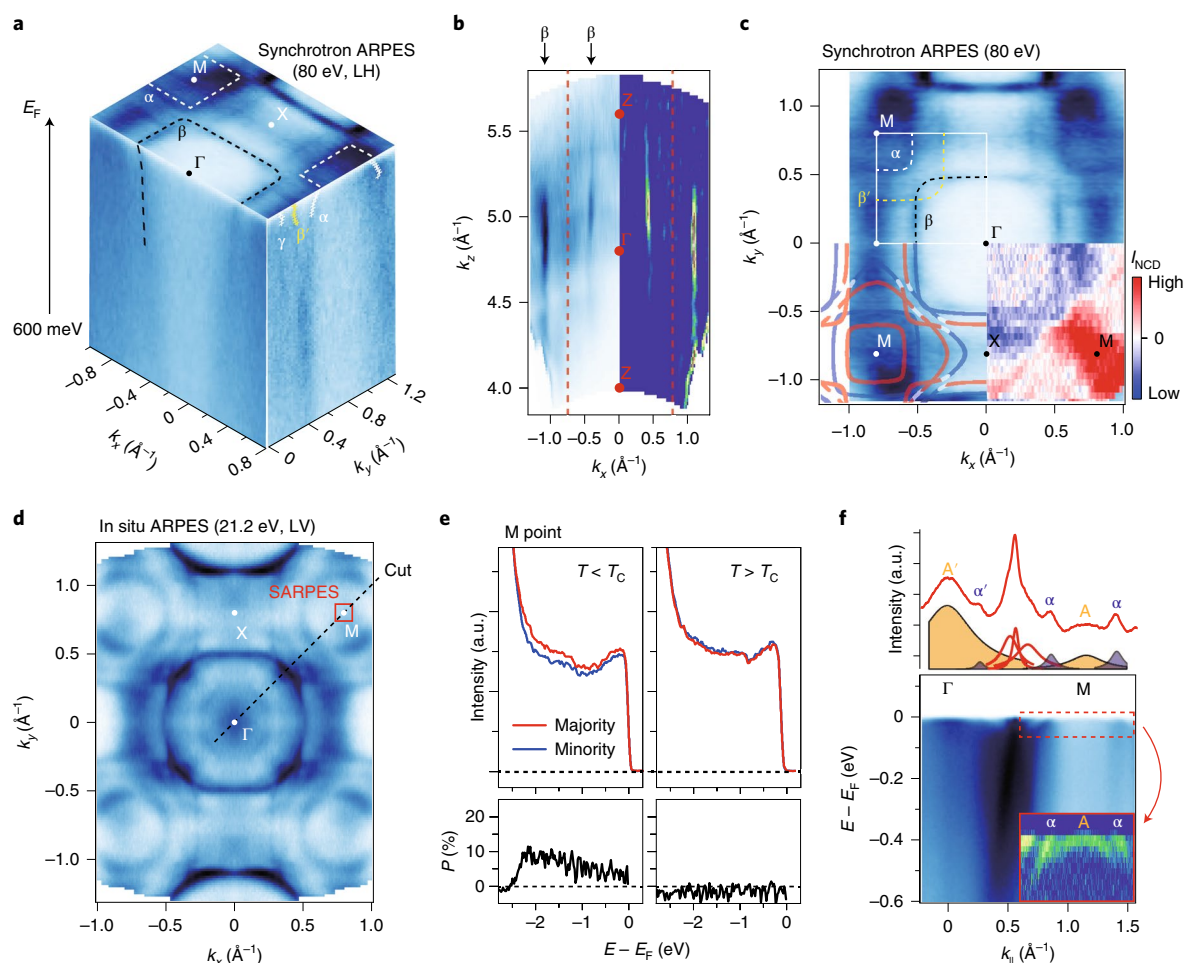


Fig. 2 | ARPES data of a 4 u.c. SRO thin film. **a**, Intensity plot of ARPES data obtained with LH polarized synchrotron light with a photon energy of 80 eV. An integration window of $E_F \pm 8$ meV is used, where E_F is the Fermi energy. The α , folded β (β') and γ bands are marked in the E - k_y cut. The folded β band is induced due to the $\sqrt{2} \times \sqrt{2}$ octahedron rotation in the tetragonal structure of SRO. **b**, FS map in the k_x - k_z plane obtained with an integration window of $E_F \pm 20$ meV (left) and its 2D curvature (right). The red dashed lines indicate the zone boundary. **c**, FS map of the data in **a**. The white, black and yellow dashed lines indicate the α , β and β' bands, respectively. The thick lines from the tight-binding model fit are superimposed on the bottom-left part of the map. Shown on the bottom right is a normalized CD FS with an integration window of $E_F \pm 27$ meV. The normalized CD (NCD) intensity is defined as $I_{\text{NCD}} = (I_{\text{RCP}} - I_{\text{LCP}}) / (I_{\text{RCP}} + I_{\text{LCP}})$, where I_{RCP} and I_{LCP} are the intensity of spectra measured with right and left circularly polarized light. **d**, FS map obtained in situ with dominantly LV-polarized He-I α light (21.2 eV). An integration range of $E_F \pm 10$ meV was used. SARPES, spin-resolved ARPES. **e**, SARPES data of the valence band at the M point. Measurements were done at 10 K ($T < T_C$) and 125 K ($T > T_C$). Lower panels show the spin polarization, P . Dashed lines indicate zero intensity. **f**, A Γ -M high-symmetry cut (lower) and a momentum distribution curve obtained by integrating $E_F \pm 10$ meV (upper). $k_{||}$ indicates the in-plane momentum along the Γ -M direction. Shown with the momentum distribution curve is its fit result with Lorentzian peaks. The blue (orange) peaks near M come from the α (A') band. Replica peaks (A' and α') appear near the Γ point due to the band folding. Inset, 2D curvature band dispersion near the M point.

SRO ultrathin films under an out-of-plane magnetic field. Here, the thickness of the thin film was estimated from the corresponding in situ reflection high-energy electron diffraction intensity plot (Supplementary Information for details). In general, the ordinary Hall effect (OHE), AHE and the hump-like features that are observed near the coercive field can contribute to the Hall resistivity ρ_{xy} , which is thus given by $\rho_{xy} = \rho_{\text{OHE}} + \rho_{\text{AHE}} + \rho_{\text{hump}}$ (refs. 24,29,30). The OHE term, which is proportional to an applied magnetic field, was subtracted from all Hall resistivity data presented in this paper. As ρ_{hump} is non-zero only near the coercive field, ρ_{AHE} can be determined from the saturated ρ_{xy} in the high-field limit.

The thickness dependence of ρ_{AHE} is shown in Fig. 3b. Here, ρ_{AHE} decreased as the thickness decreased and eventually took on a negative value with a sign change in between. We also performed ionic liquid gating of SRO ultrathin films to investigate how the change in the chemical potential affects ρ_{xy} . Figure 3c shows the results of ionic

gating experiments for 4 and 5 u.c. SRO thin films measured at 10 and 50 K, respectively. In both cases, the magnitude of ρ_{xy} changed substantially with the gate voltage. Figure 3d shows the out-of-plane magnetization of 4, 5 and 7 u.c. SRO thin films. Combining the thickness- and temperature-dependent Hall effect results with the magnetization (M) data, we can derive ρ_{AHE} versus M data, as plotted in Fig. 3e (Supplementary Information for details). It should be noted that the data points fall on a single line, implying that M may be the key parameter for ρ_{AHE} . The sign reversal of ρ_{AHE} can also be clearly observed as the magnetization approaches $0.5 \mu_B$ per Ru, where μ_B is the Bohr magneton.

The 2D symmetry-protected nodal structures

It is worth noting that the sign-switching behaviour of ρ_{AHE} is highly unusual¹⁰. To understand the origin of the unusual AHE, we conducted a tight-binding model analysis combined with

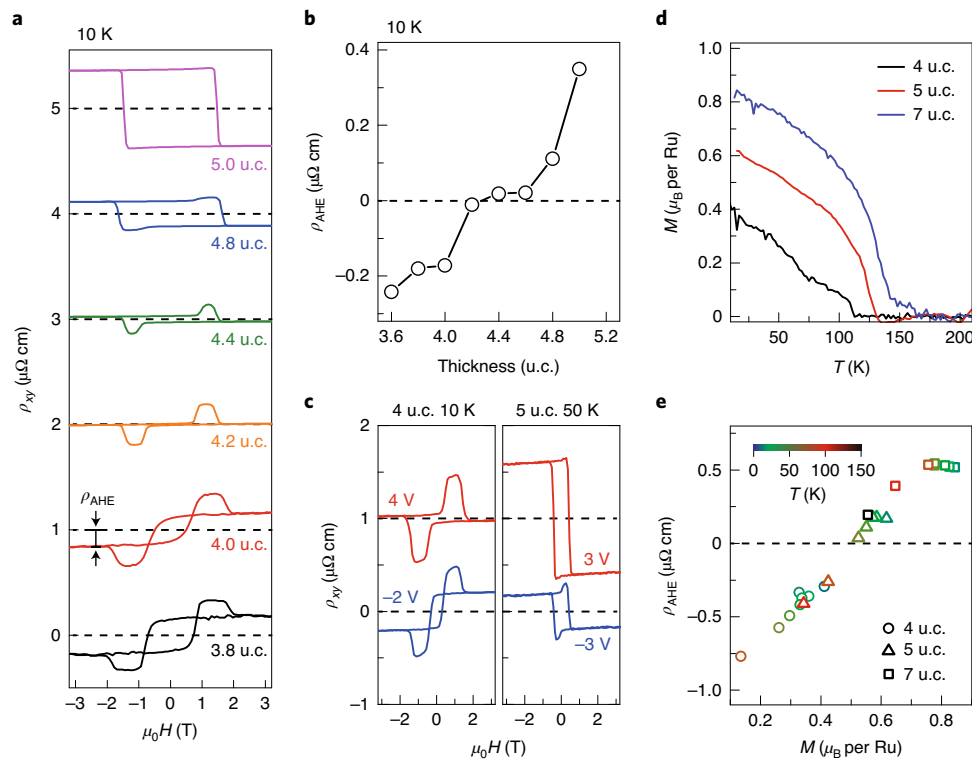


Fig. 3 | Non-monotonous AHE in SRO ultrathin films. **a**, Thickness-dependent ρ_{xy} of SRO ultrathin films at 10 K as a function of magnetic field (H); ρ_{AHE} is defined from the saturated Hall resistivity ρ_{xy} . μ_0 is the vacuum permeability. **b**, The ρ_{AHE} versus thickness curve for SRO ultrathin films at 10 K. The sign of ρ_{AHE} changes as the film thickness varies. **c**, The ρ_{xy} of 4 and 5 u.c. SRO thin films with ionic liquid gating at 10 and 50 K, respectively. The sign and magnitude of ρ_{AHE} change with the bias voltage. **d**, Out-of-plane magnetization of 4, 5 and 7 u.c. SRO thin films. **e**, The ρ_{AHE} versus M plot for 4, 5 and 7 u.c. SRO thin films at various temperatures. The sign of ρ_{AHE} changes near $0.5 \mu_B$ per Ru.

first-principles calculations. Figure 4a shows the band structure in the effective six-band tight-binding model (relevant to a 1 u.c. SRO), the parameters of which were adjusted to describe the FS in Fig. 2c with a magnetization $M = 0.33 \mu_B$ per Ru. With magnetization and SOC, several bands are hybridized near the points at which they are crossed. We find that two different origins of symmetry-protected nodal structures, which we call a NL (white circle) and QBC (black circle), are formed at the crossing points. The NLs and QBCs of spin-polarized bands, respectively, become the sources of the large Berry curvature when they are gapped due to SOC. We note that the lowest lying QBC band at the M point is the A band that we observed in Fig. 2f.

To explain the characteristics of a NL and QBC in detail, a band structure along the M–X–M line is presented in Fig. 4b. For simplicity, we focus on three out of the six bands, in which two majority bands are derived from $d_{xz,yz}$ orbitals (red) and one minority band originates from the d_{xy} orbital (blue). The properties of the system as a whole can be understood simply by doubling the number of bands.

When the crossing between bands with opposite spin polarization exists, it generally leads to 2D NLs in spin-polarized systems^{31,32}. In the absence of SOC, the majority and minority bands are not hybridized, so that NLs form when they intersect³². Meanwhile, due to the tetragonal crystalline symmetry of thin films, QBCs can appear at the Γ and M points with C_{4v} point group symmetry made up of bands with the same spin character^{33,34}. These NLs and QBCs are generic nodal structures that exist in the spin-polarized bands of layered 2D perovskite structures (Methods for details). Figure 4c shows the configuration of NLs and QBCs in the momentum space formed by three out of the six bands in Fig. 4b. When SOC is turned

on, these nodal structures are gapped and Berry curvature is thus generated, which leads to the AHE (Methods for details).

Sign-changing AHE

Multiple Berry curvature sources appearing near the Fermi level can induce a fluctuating Berry curvature distribution with alternating signs. The upper half of Fig. 5a shows that QBCs formed by minority bands induce negative Berry curvature while the others generate positive Berry curvature. For better visualization, we plot the Berry curvature distribution of a 1 u.c. SRO in Fig. 5b. The resulting Berry curvature distribution is similar to a previously reported one³.

Since the sign-alternating Berry curvature distribution is generated by the topological band crossings, it would be desirable to experimentally show the Berry curvature behaviour in the momentum space. During the past decade, the connection between Berry curvature and orbital angular momentum (OAM) has been firmly established^{35,36}. In addition, measurement of OAM (and thus Berry curvature) with CD-ARPES has been well studied^{37–39}. In fact, CD-ARPES has been used to study chiral structures of pseudo-spins of topological bands^{11,38,39}. Therefore, the CD-ARPES in Fig. 2c may be compared with the calculated OAM of our 1 u.c. tight-binding model. The upper half of Fig. 5c shows a clear match between the CD-ARPES data and OAM distribution. Positive CD intensity and OAM are observed near the M point, but they turn negative away from the M point. Eventually, both experimental and theoretical results turn to zero close to the Γ point. Interestingly, we found that both the calculated OAM and Berry curvature flip their signs along the Γ –M high-symmetry line due to the intrinsic nature of QBC (Methods for the relationship between OAM and Berry curvature).

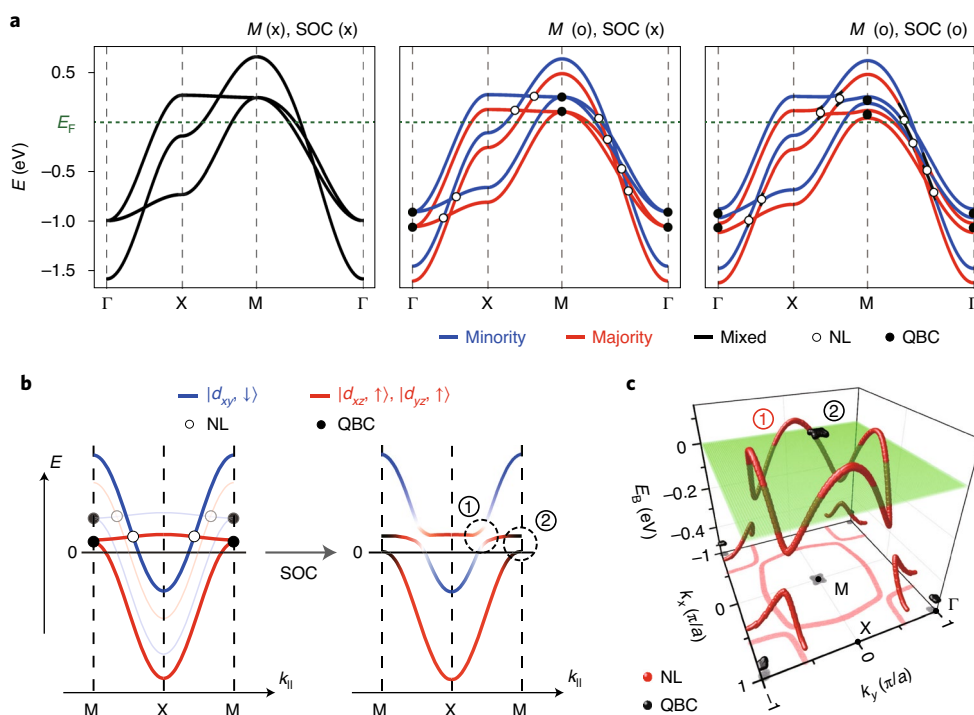


Fig. 4 | Mechanism for the sign-tunable AHE induced by NLs and nodal points in a 2D ferromagnetic perovskite. **a**, Band structures of SRO calculated from an effective six-band model relevant to 1 u.c. SRO. o and x indicate with and without M or SOC. Without SOC, QBCs appear at the Γ and M points, and NLs are formed when majority and minority bands cross. **b**, A calculated band structure along the M-X-M line. For easier understanding, we focus on the two majority bands derived from $d_{xz,yz}$ orbitals (red) and the one minority band from the d_{xy} orbital (blue). QBC occurs at the M point and an NL is formed when the majority and minority bands cross. SOC can lift the degeneracy of the nodal structures, as denoted by circled numbers in the right panel. In **a**, **b** and Fig. 5a, a white (black) circle denotes a source of Berry curvature from the NL (QBC). **c**, Configuration of nodal structures in the momentum space. Red lines (black dots) denote the NLs (QBCs). E_b and a are $E - E_F$ and in-plane lattice constant of SRO, respectively.

To demonstrate that the QBCs and NLs are present, and also that the associated sign-switching of the AHE signal is a generic property of SRO ultrathin films independent of film thickness, we also constructed a tight-binding model for 4 u.c. SRO and compared it with the effective six-band model. The hopping parameters for the 4 u.c. tight-binding Hamiltonian were extracted from first-principles calculations and adjusted further by fitting the experimentally observed FSs. For realistic calculations, the atomic positions of 4 u.c. SRO were obtained from the experiment using coherent Bragg rod analysis²⁴ (Methods for the detailed description of the model). The lower half of Fig. 5a shows the FS and Berry curvature derived from the 4 u.c. model, where large Berry curvatures are generated by gapped QBCs and NLs. The 1 u.c. and 4 u.c. models predict similar FS and Berry curvature distributions. Both models also show consistent OAM distributions, as shown in the right half in Fig. 5c.

Due to multiple sources of enhanced Berry curvature generated by QBCs and NLs, as shown in Figs. 5a,b, the sign and magnitude of the AHE can vary depending on the energies of the nodal structures relative to the Fermi level (Methods for details). We show that the sign and magnitude of the AHE can be controlled by different parameters, such as the magnetization and chemical potential. The calculated anomalous Hall conductivity (AHC), $\sigma_{\text{AHE}} = \rho_{xy}/(\rho_{xy}^2 + \rho_{xx}^2)$, where ρ_{xx} (ρ_{xy}) is the resistivity (Hall resistivity), using two tight-binding models for 1 u.c. and 4 u.c. SRO as a function of magnetization, matches well with the experimental results (Fig. 5d). The sign of the AHC reverses when the amplitude of the magnetization varies. Note that the sign-switching AHC appears in both the 1 u.c. and 4 u.c. models.

The chemical potential dependence of the AHC was also computed using the tight-binding model (Fig. 5e). According to the calculation with $M \approx 0.4 \mu_B$ per Ru, the AHC increases with the chemical potential. This tendency is in accordance with the ionic liquid gating measurements on 4 and 5 u.c. SRO ultrathin films (Fig. 5e, inset). Given that both films have a magnetization of $M \approx 0.4 \mu_B$ per Ru, AHC tends to increase as the gate voltage increases. We believe that these results can support that the sign-changing AHE comes from competition between Berry curvature sources from multiple topological features as magnetization and chemical potential change. In particular, we found that as the chemical potential increases, the positive Berry curvatures from the NL and majority band QBC dominate the negative Berry curvature from the minority band QBC, which eventually leads to the sign reversal of the AHC. Interestingly, the AHC is not proportional to the net magnetization, and the sign of the AHC can change with a small variation of magnetization and chemical potential, as schematically shown in Fig. 5f.

In past decades, the non-monotonous AHE of SRO has been studied not only in the ultrathin limit (that is, the 2D limit)^{3,24,29,40}, but also in the 3D limit, like single crystals and thick films^{10,41}. Interestingly, the sign-changing AHE versus magnetization in the 2D SRO shows a similar tendency to that of 3D SROs. Such a similarity of the AHE between 2D and 3D SROs is quite surprising because 3D topological band structure is generally not adiabatically connected to the band structure of 2D layers. As the interlayer coupling generates several band inversion processes, which strongly modify the nodal structures, the topological nodal structures and related Berry curvature distribution of 2D and 3D materials are not smoothly connected in

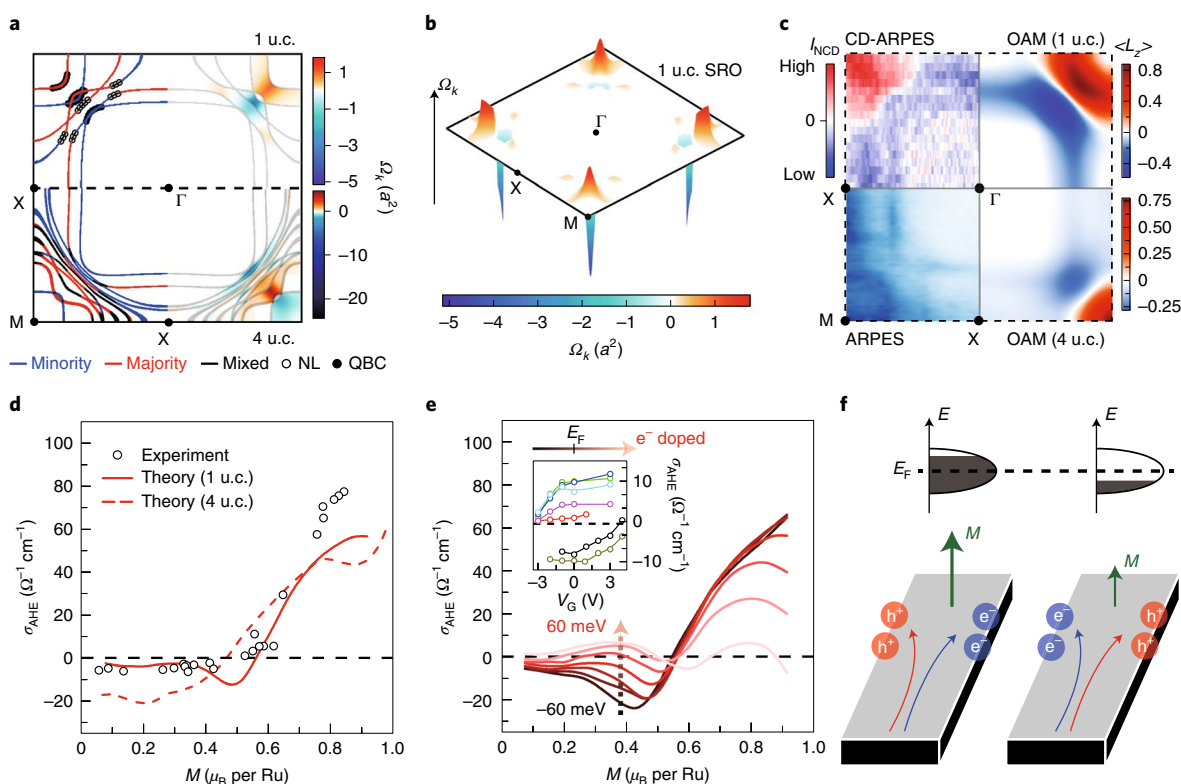


Fig. 5 | Berry curvature hot spots from nodal structures and switchable AHE of the SRO ultrathin film. **a**, Calculated band structure and Berry curvature (Ω_k) of SRO at the Fermi level. SOC is turned on. While the majority (blue) and minority (red) bands are spin polarized, the mixed bands (black lines) have comparable contributions from up and down spins. The upper (lower) half of the figure is derived from the 1 u.c. (4 u.c.) tight-binding model. The left (right) half of the figure indicates the band structures (Berry curvature distribution) at the Fermi level. a is the in-plane lattice constant of SRO. **b**, Calculated Berry curvature distribution of 1 u.c. SRO in momentum space. **c**, CD-ARPES (top left) and normal ARPES (bottom left) FSs. OAM at the Fermi level from the tight-binding model of 1 u.c. (top right) and 4 u.c. (bottom right) SRO. $\langle L_z \rangle$ is the expectation value of the out-of-plane OAM component. **d**, Measured (circles) and calculated (solid (dashed) line for the 1 u.c. (4 u.c.) model) magnetization dependence of the AHC. When the magnetization is small (large), the AHC is negative (positive). **e**, Chemical potential dependence of the AHC. The AHC increases with the chemical potential as the magnetization is about $0.4 \mu_B$ per Ru. Inset, ionic liquid gating measurements on 4 and 5 u.c. SRO thin films. The AHC increases with the gate voltage (V_G). e^- , electron. **f**, A schematic showing the sign-tunable AHE. The sign of the anomalous Hall resistivity can change as the magnetization or Fermi energy is varied due to Berry curvature hot spots near the Fermi level induced by nodal structures. h^+ , hole.

general. Especially, QBCs and NLs of 2D SRO cannot be understood from a simple 2D confinement of magnetic monopoles in 3D SRO. The generic evolution pattern of the band structure between the 2D and 3D limits is further examined using the tight-binding model shown in the Supplementary Information.

Because the topological nodal structures (QBCs and NLs) are protected only by symmetries, similar nodal structures can appear in any 2D systems sharing the same space group symmetry as SRO. To confirm this idea, we also performed first-principles calculations on monolayer SrCoO_3 , another ferromagnetic perovskite oxide, in which the sign-switching AHE was recently observed in thin films⁴². Interestingly, the NLs and QBCs were also located close to the Fermi energy and generated Berry curvatures with opposite signs, as in SRO (Supplementary Information for details).

Let us briefly mention the stability of NLs and QBCs under rotation or tilting of oxygen octahedra. NLs are stable against rotation or tilting as they do not affect spins when SOC is absent. QBCs are stable against rotation distortion that preserves C_4 rotation. Although the tilting breaks the C_4 symmetry, the topological properties of QBCs should still remain intact as long as the SOC-induced gap is larger than the gap caused by tilting. We believe that a similar mechanism may be applicable to understanding the mysterious AHE in other ferromagnetic perovskite oxides and emergent interfacial ferromagnetism.

Outlook

In conclusion, by combining ARPES, transport measurements and theoretical analysis, we demonstrated the topological band structure of ferromagnetic SRO thin films. In particular, the band structures of a SRO film in the ultrathin 2D limit were observed and defined. Through theoretical analysis, we also showed that the spin-polarized bands of 2D ferromagnets generally possess nodal points and NLs that become the source of enhanced Berry curvature. Comparing the measured band structure with the tight-binding model, we identified the Berry curvature hot spots originating from multi-nodal structures, which led to the unconventional AHE. Competing contributions from different Berry curvature hot spots induce a sign-changing AHE, which can be controlled by varying the film thickness, temperature, magnetization and chemical potential. We believe that our findings will open up new avenues for investigating transport phenomena driven by symmetry-protected nodal structures of 2D magnetic systems, and facilitate the development of magnetic devices based on the engineering of magnetic topological band structures.

Online content

Any methods, additional references, Nature Research reporting summaries, source data, extended data, supplementary information, acknowledgements, peer review information; details of author

contributions and competing interests; and statements of data and code availability are available at <https://doi.org/10.1038/s41563-021-01101-4>.

Received: 5 December 2019; Accepted: 11 August 2021;

References

- Burkov, A. A. Anomalous Hall effect in Weyl metals. *Phys. Rev. Lett.* **113**, 187202 (2014).
- Ye, L. et al. Massive Dirac fermions in a ferromagnetic kagome metal. *Nature* **555**, 638–642 (2018).
- Groenendijk, D. J. et al. Berry phase engineering at oxide interfaces. *Phys. Rev. Res.* **2**, 023404 (2020).
- Chang, G. et al. Room-temperature magnetic topological Weyl fermion and nodal line semimetal states in half-metallic Heusler Co_2TiX (X = Si, Ge, or Sn). *Sci. Rep.* **6**, 38839 (2016).
- Chang, G. et al. Magnetic and noncentrosymmetric Weyl fermion semimetals in the RAlGe family of compounds (R = rare earth). *Phys. Rev. B* **97**, 041104 (2018).
- Kim, K. et al. Large anomalous Hall current induced by topological nodal lines in a ferromagnetic van der Waals semimetal. *Nat. Mater.* **17**, 794–799 (2018).
- Nagaosa, N., Sinova, J., Onoda, S., MacDonald, A. H. & Ong, N. P. Anomalous Hall effect. *Rev. Mod. Phys.* **82**, 1539–1592 (2010).
- Zeng, C., Yao, Y., Niu, Q. & Weitering, H. H. Linear magnetization dependence of the intrinsic anomalous Hall effect. *Phys. Rev. Lett.* **96**, 037204 (2006).
- Wang, Q. et al. Large intrinsic anomalous Hall effect in half-metallic ferromagnet $\text{Co}_3\text{Sn}_2\text{S}_2$ with magnetic Weyl fermions. *Nat. Commun.* **9**, 3681 (2018).
- Fang, Z. et al. The anomalous Hall effect and magnetic monopoles in momentum space. *Science* **302**, 92–95 (2003).
- Chen, Y., Bergman, D. & Burkov, A. Weyl fermions and the anomalous Hall effect in metallic ferromagnets. *Phys. Rev. B* **88**, 125110 (2013).
- Vazifeh, M. M. & Franz, M. Electromagnetic response of Weyl semimetals. *Phys. Rev. Lett.* **111**, 027201 (2013).
- Zyuzin, A. A. & Tiwari, R. P. Intrinsic anomalous Hall effect in type-II Weyl semimetals. *JETP Lett.* **103**, 717–722 (2016).
- Young, S. M. & Kane, C. L. Dirac semimetals in two dimensions. *Phys. Rev. Lett.* **115**, 126803 (2015).
- Niu, C. et al. Two-dimensional topological nodal line semimetal in layered X_2Y (X = Ca, Sr, and Ba; Y = As, Sb, and Bi). *Phys. Rev. B* **95**, 235138 (2017).
- Zhang, H., Huang, H., Haule, K. & Vanderbilt, D. Quantum anomalous Hall phase in (001) double-perovskite monolayers via intersite spin-orbit coupling. *Phys. Rev. B* **90**, 165143 (2014).
- Wan, X., Turner, A. M., Vishwanath, A. & Savrasov, S. Y. Topological semimetal and Fermi-arc surface states in the electronic structure of pyrochlore iridates. *Phys. Rev. B* **83**, 205101 (2011).
- Neumeier, J. et al. Magnetic, thermal, transport, and structural properties of $\text{Sr}_2\text{RuO}_{4+\delta}$: enhanced charge-carrier mass in a nearly metallic oxide. *Phys. Rev. B* **50**, 17910 (1994).
- Puchkov, A., Shen, Z.-X., Kimura, T. & Tokura, Y. ARPES results on Sr_2RuO_4 : Fermi surface revisited. *Phys. Rev. B* **58**, R13322 (1998).
- Damascelli, A. et al. Fermi surface, surface states, and surface reconstruction in Sr_2RuO_4 . *Phys. Rev. Lett.* **85**, 5194–5197 (2000).
- Mackenzie, A. P. et al. Quantum oscillations in the layered perovskite superconductor Sr_2RuO_4 . *Phys. Rev. Lett.* **76**, 3786–3789 (1996).
- Mackenzie, A. P. et al. The Fermi surface topography of Sr_2RuO_4 . *J. Phys. Soc. Jpn* **67**, 385–388 (1998).
- Chang, S. H. et al. Thickness-dependent structural phase transition of strained SrRuO_3 ultrathin films: the role of octahedral tilt. *Phys. Rev. B* **84**, 104101 (2011).
- Sohn, B. et al. Stable hump-like Hall effect and noncoplanar spin textures in SrRuO_3 ultrathin films. *Phys. Rev. Res.* **3**, 023232 (2021).
- Singh, D. & Mazin, I. Electronic structure and magnetism of $\text{Sr}_3\text{Ru}_2\text{O}_7$. *Phys. Rev. B* **63**, 165101 (2001).
- Chang, Y. J. et al. Fundamental thickness limit of itinerant ferromagnetic SrRuO_3 . *Phys. Rev. Lett.* **103**, 057201 (2009).
- Jeong, D. W. et al. Temperature evolution of itinerant ferromagnetism in SrRuO_3 probed by optical spectroscopy. *Phys. Rev. Lett.* **110**, 247202 (2013).
- Zhang, P. et al. A precise method for visualizing dispersive features in image plots. *Rev. Sci. Instrum.* **82**, 043712 (2011).
- Matsuno, J. et al. Interface-driven topological Hall effect in SrRuO_3 - SrIrO_3 bilayer. *Sci. Adv.* **2**, e1600304 (2016).
- Sohn, B. et al. Hump-like structure in Hall signal from ultra-thin SrRuO_3 films without inhomogeneous anomalous Hall effect. *Curr. Appl. Phys.* **20**, 186–190 (2020).
- Jin, L. et al. Two-dimensional Weyl nodal-line semimetal in a d^0 ferromagnetic K_2N monolayer with a high Curie temperature. *Phys. Rev. B* **102**, 125118 (2020).
- Jin, L. et al. Ferromagnetic two-dimensional metal-chlorides MCl (M = Sc, Y, and La): candidates for Weyl nodal line semimetals with small spin-orbit coupling gaps. *Appl. Surf. Sci.* **520**, 146376 (2020).
- Sun, K., Yao, H., Fradkin, E. & Kivelson, S. A. Topological insulators and nematic phases from spontaneous symmetry breaking in 2D Fermi systems with a quadratic band crossing. *Phys. Rev. Lett.* **103**, 046811 (2009).
- Chong, Y. D., Wen, X.-G. & Soljačić, M. Effective theory of quadratic degeneracies. *Phys. Rev. B* **77**, 235125 (2008).
- Xiao, D., Yao, W. & Niu, Q. Valley-contrasting physics in graphene: magnetic moment and topological transport. *Phys. Rev. Lett.* **99**, 236809 (2007).
- Go, D., Jo, D., Kim, C. & Lee, H.-W. Intrinsic spin and orbital Hall effects from orbital texture. *Phys. Rev. Lett.* **121**, 086602 (2018).
- Cho, S. et al. Experimental observation of hidden Berry curvature in inversion-symmetric bulk 2H-WS_2 . *Phys. Rev. Lett.* **121**, 186401 (2018).
- Park, S. R. et al. Chiral orbital-angular momentum in the surface states of Bi_2Se_3 . *Phys. Rev. Lett.* **108**, 046805 (2012).
- Schüler, M. et al. Local Berry curvature signatures in dichroic angle-resolved photoelectron spectroscopy from two-dimensional materials. *Sci. Adv.* **6**, eaay2730 (2020).
- Schultz, M., Levy, S., Reiner, J. W. & Klein, L. Magnetic and transport properties of epitaxial films of SrRuO_3 in the ultrathin limit. *Phys. Rev. B* **79**, 125444 (2009).
- Mathieu, R. et al. Scaling of the anomalous Hall effect in $\text{Sr}_{1-x}\text{Ca}_x\text{RuO}_3$. *Phys. Rev. Lett.* **93**, 016602 (2004).
- Zhang, D. et al. Origin of the anomalous Hall effect in SrCoO_3 thin films. *Phys. Rev. B* **100**, 060403 (2019).

Publisher's note Springer Nature remains neutral with regard to jurisdictional claims in published maps and institutional affiliations.

© The Author(s), under exclusive licence to Springer Nature Limited 2021

Methods

SRO thin-film fabrication. SRO ultrathin films were grown on TiO₂-terminated SrTiO₃ (STO) (001) single-crystal substrates using pulsed laser deposition. TiO₂-terminated STO substrates from Shinkosha were used for SRO thin-film growth. To dissolve the Sr compounds that can form on the surface of STO substrates, the STO substrates were prepared by deionized water etching. The deionized water-treated STO substrates were preannealed in situ at 1,070 °C for 30 min with an oxygen partial pressure (PO₂) of 5×10^{-6} torr. We deposited an epitaxial SRO thin film in an oxygen partial pressure of PO₂ = 100 mtorr; the growth temperature of the STO substrate was 700 °C. A KrF excimer laser (wavelength, 248 nm) irradiated a stoichiometric SRO target with a fluence of $1\text{--}2 \text{ J cm}^{-2}$ and repetition rate of 2 Hz. Reflection high-energy electron diffraction was used to monitor the growth dynamics. To clean the surface of SRO thin films, we postannealed them at 550 °C for 10 min.

Transport and magnetic measurements. For the Hall effect measurement of SRO thin films, we prepared a 60-nm-thick Au electrode on top of the SRO thin films with a Hall bar geometry using an electron beam evaporator. Electric transport measurement was carried out using a physical property measurement system (Quantum Design). The magnetic characterization was performed using superconducting quantum interface device magnetometry with out-of-plane geometry. Given that the easy axis of the SRO ultrathin film is perpendicular to the thin film on the STO (001) substrate, we measured the out-of-plane magnetization via superconducting quantum interface device magnetometry^{24,40}. For ionic liquid gating, we used diethylmethyl(2-methoxyethyl)ammonium bis(trifluoromethylsulfonyl)imide as an electrolyte. We applied a gate voltage at 260 K for 30 min to form an electric double layer.

ARPES. In situ ARPES measurements were performed at 10 K using the home lab system equipped with a Scienta DA30 analyser and a discharge lamp from Fermi Instruments. He-I α ($E_{\text{ph}} = 21.2 \text{ eV}$, where E_{ph} is the photon energy) light was mostly used. For the photon-energy-dependent and CD studies, ARPES measurements were performed at the beamline 4.0.3 end station of the Advanced Light Source equipped with a Scienta R8000. Photon-energy-dependent ARPES measurements were performed at 10 K with photon energies ranging from 50 to 120 eV. CD-ARPES measurements were performed at 20 K with left- and right-circularly polarized 80 eV light. The light incident angle was $45 \pm 10^\circ$.

Spin polarization was measured with a spin-resolved ARPES system in our laboratory. The system was equipped with a SPECS PHOIBOS 225 analyser and a very low-energy electron diffraction spin detector. For the spin detector, an oxidized iron film deposited on W (100) was used as the scattering target. He-I α ($h\nu = 21.2 \text{ eV}$) light was used as the light source. The energy resolution was set to $\sim 60 \text{ meV}$ with a pass energy of 10 eV. We used a Sherman function value of 0.29 ± 0.01 to obtain the spin polarization.

First-principles calculations. We performed first-principles density functional theory (DFT) calculations with the generalized gradient approximation using the Vienna Ab-initio Simulation Package⁴³. Perdew–Burke–Ernzerhof parametrization⁴⁴ for the exchange–correlation functional and the projector augmented wave method⁴⁵ were used, with an energy cut-off of 500 eV and a k -point sampling on an $8 \times 8 \times 1$ grid. The electronic structures of a 4 u.c. SRO film were obtained by analysing a slab of the SRO/STO heterostructure consisting of 4 layers of SRO and 4.5 layers of STO (including an additional SrO at the surface) and a vacuum of 19 Å. We used the atomic positions obtained from the experiment using coherent Bragg rod analysis²⁴, having a $\sqrt{2} \times \sqrt{2}$ in-plane unit cell to include octahedral rotation. The ferromagnetic ground state was obtained with an average Ru magnetic moment of $1.2 \mu_B$. The tight-binding parameters for Ru- d -derived bands of the SRO/STO heterostructure were obtained using the Wannier90 package⁴⁶. For the generalized gradient approximation plus U calculations presented in the Supplementary Information, we used the rotationally invariant form of the on-site Coulomb interaction⁴⁷ with $U = 3.23 \text{ eV}$ and $J = 0.74 \text{ eV}$ (where U and J are on-site Coulomb energy and Hund's exchange coupling, respectively) from constrained random-phase approximation calculation⁴⁸.

The electronic structure of 2D SrCoO₃ was calculated using a slab geometry of 1.5 layers of SrCoO₃ (including an additional SrO layer at the surface) with a vacuum of 10 Å in which the experimental atomic positions of bulk SrCoO₃ were used⁴⁹. The space group of the atomic structure including the vacuum was $P4/mmm$ (124). The energy cut-off of 600 eV and k -point sampling on a $10 \times 10 \times 1$ grid were used. SOC was included. The ferromagnetic ground state was obtained with the Co magnetic moment of $1.6 \mu_B$, in which the out-of-plane magnetization direction was preferred with a magnetic anisotropy energy of 1 meV. The Berry curvature was calculated using the Wannier90 package⁴⁶ based on the tight-binding Hamiltonian constructed from the Wannier functions of Co- d - and O- p -derived bands.

Effective tight-binding model for monolayer SRO. In the main text, we assumed that the electronic structure of 4 u.c. SRO can be described well by effective 2D models, which are supported by k_z -dependent ARPES measurement. Following the

Slater–Koster method, the tight-binding Hamiltonian of ferromagnetic monolayer SRO is constructed as follows:

$$H = \sum_{\mathbf{k}} [(\epsilon_{\mathbf{k}\sigma}^a) \delta_{ab} \delta_{\sigma\sigma'} + f_{\mathbf{k}}^{ab} \delta_{\sigma\sigma'} + i\lambda e^{abc} \tau_{\sigma\sigma'}^c] d_{\mathbf{k}a\sigma}^\dagger d_{\mathbf{k}b\sigma}, \quad (1)$$

where $a, b, c \in \{1, 2, 3\}$; \mathbf{k} is the momentum vector; σ and σ' represent spin; $d_{\mathbf{k}a\sigma}^{(\dagger)}$ is the creation (annihilation) operator of t_{2g} orbitals; and δ_{ab} and $\delta_{\sigma\sigma'}$ are Kronecker delta symbols; and e^{abc} is the Levi-Civita symbol. Also,

$$\begin{aligned} \epsilon_{\mathbf{k}\sigma}^{1=yz} &= -2t_1 \cos k_y - 2t_2 \cos k_x - 4t_3 \cos k_x \cos k_y - m\tau_{\sigma\sigma}^z, \\ \epsilon_{\mathbf{k}\sigma}^{2=xz} &= -2t_1 \cos k_x - 2t_2 \cos k_y - 4t_3 \cos k_x \cos k_y - m\tau_{\sigma\sigma}^z, \\ \epsilon_{\mathbf{k}\sigma}^{3=xy} &= -2t_1 (\cos k_x + \cos k_y) - 4t_4 \cos k_x \cos k_y - m\tau_{\sigma\sigma}^z, \\ f_{\mathbf{k}}^{12} &= -4f \sin k_x \sin k_y = f_{\mathbf{k}}^{21}, \end{aligned} \quad (2)$$

where $\epsilon_{\mathbf{k}\sigma}^a$ is the onsite energy; t_1 and t_2 are the amplitudes for nearest-neighbour interactions; t_3 , t_4 and $f_{\mathbf{k}}^{ab}$ are the amplitudes of next-nearest-neighbour interactions; λ denotes the amplitude of SOC; m is the amplitude of the Zeeman interaction; and $\tau_{\sigma\sigma'}^c$ is the Pauli matrix. For example, $\tau_{\sigma\sigma'}^z = \pm 1$ if $\sigma = \pm 1$. We fit tight-binding parameters with ARPES data to describe the AHC quantitatively (Table 1).

With the Hamiltonian, we can directly calculate the Berry curvature of each energy band $\Omega_n(\mathbf{k})$ by applying the following formula:

$$\Omega_n(\mathbf{k}) = i \sum_{n' \neq n} \frac{\langle n | \partial H / \partial k_x | n' \rangle \langle n' | \partial H / \partial k_y | n \rangle - (x \leftrightarrow y)}{(\epsilon_n(\mathbf{k}) - \epsilon_{n'}(\mathbf{k}))^2}, \quad (3)$$

where $\epsilon_{n(n')}$ is the energy of the $n(n')$ th band represented by $|n\rangle$ ($|n'\rangle$). The AHC σ_{xy} is given by integrating the Berry curvature over the Brillouin zone below the Fermi energy:

$$\sigma_{xy} = \frac{c}{2\pi} \sum_{n=1}^N \int dk_x dk_y \Omega_n(\mathbf{k}) \theta(\epsilon_n(\mathbf{k}) - E_F), \quad (4)$$

where $\theta(x)$ is step function that is 0 (1) when $x \geq 0$ ($x < 0$). Also, $c = (R_H \times l)^{-1}$, where R_H is the Hall resistance and l is the thickness of the SRO thin film.

Tight-binding model for 4 u.c. SRO. We construct the 4 u.c. SRO tight-binding model where the parameters are extracted from the DFT calculation and adjusted further by fitting the experimentally observed FSs. The DFT calculation is performed based on the structure of 4 u.c. SRO ultrathin films, where the atomic structure information is obtained by coherent Bragg rod analysis that determines the layer-by-layer atomic positions of SRO ultrathin films. In the tight-binding Hamiltonian, only t_{2g} orbitals are considered since they account for most of the density of states near the Fermi level. Also, the tiny lattice rotation is neglected and the tetragonal structure is assumed. The Hamiltonian $\hat{H} = \psi^\dagger H \psi$ is described by the matrix H and the basis ψ and its complex conjugate ψ^* , where

$$H = \begin{bmatrix} E_1 & t_{12} & 0 & 0 \\ t_{12}^\dagger & E_2 & t_{23} & 0 \\ 0 & t_{32}^\dagger & E_3 & t_{34} \\ 0 & 0 & t_{34}^\dagger & E_4 \end{bmatrix}, \quad (5)$$

$$\psi^\dagger = (d_{1,\mathbf{k}a\sigma}^\dagger, d_{2,\mathbf{k}a\sigma}^\dagger, d_{3,\mathbf{k}a\sigma}^\dagger, d_{4,\mathbf{k}a\sigma}^\dagger). \quad (6)$$

Here E_n describes the intralayer part of the Hamiltonian $E_n d_{n,\mathbf{k}a\sigma}^\dagger d_{n,\mathbf{k}b\sigma}$ where n denotes the index for the SRO layer. The t_{nm} and t_{mn}^* describe the hopping interaction between n th layer and m th layer. Let us note that $t_{nm} = t_{mn}^*$, due to the Hermiticity of the Hamiltonian.

The intralayer Hamiltonian $\hat{H}_{n,\text{intra}} = E_n d_{n,\mathbf{k}a\sigma}^\dagger d_{n,\mathbf{k}b\sigma}$ is written as

$$\hat{H}_{n,\text{intra}} = \sum_{\mathbf{k}} [(\epsilon_{n,\mathbf{k}\sigma}^a) \delta_{ab} \delta_{\sigma\sigma'} + f_{\mathbf{k}}^{ab} \delta_{\sigma\sigma'} + i\lambda e^{abc} \tau_{\sigma\sigma'}^c] d_{n,\mathbf{k}a\sigma}^\dagger d_{n,\mathbf{k}b\sigma}, \quad (7)$$

where

$$\begin{aligned} \epsilon_{n,\mathbf{k}\sigma}^{1=yz} &= -2t_{1,n} \cos k_y - 2t_{2,n} \cos k_x - m\tau_{\sigma\sigma}^z, \\ \epsilon_{n,\mathbf{k}\sigma}^{2=xz} &= -2t_{1,n} \cos k_x - 2t_{2,n} \cos k_y - m\tau_{\sigma\sigma}^z, \\ \epsilon_{n,\mathbf{k}\sigma}^{3=xy} &= U - 2t_{3,n} (\cos k_x + \cos k_y) - 4t_{4,n} \cos k_x \cos k_y \\ &\quad - m\tau_{\sigma\sigma}^z, \\ f_{\mathbf{k}}^{12} &= -4f \sin k_x \sin k_y = f_{\mathbf{k}}^{21}, \end{aligned} \quad (8)$$

Table 1 | Parameters for tight-binding model Hamiltonian describing 1 u.c. SRO

E_f (eV)	t_1 (eV)	t_2 (eV)	t_3 (eV)	t_4 (eV)	m (eV)	f (eV)	λ (eV)	$M\mu_B$ per Ru
0.3	0.28	0.03	0.018	0.04	0.08	0.015	0.045	0.33

Table 2 | Parameters for 4 u.c. effective tight-binding model Hamiltonian

	$t_{1,n}$ (eV)	$t_{2,n}$ (eV)	$t_{3,n}$ (eV)	$t_{4,n}$ (eV)	U (eV)	$u_{1,n}$ (eV)	$u_{2,n}$ (eV)	f (eV)	λ (eV)	E_f (eV)
$n=1$	0.367	-0.03	0.35	0.12		0.320	0.15			
$n=2$	0.348	-0.03	0.35	0.12	0.2	0.253	0.15	-0.03	0.06	0.75
$n=3$	0.290	-0.03	0.30	0.10		0.213	0.15			
$n=4$	0.250	-0.03	0.25	0.01						

where $t_{1,n}$, $t_{2,n}$ and $t_{3,n}$ are the amplitudes of the nearest-neighbour interactions and $t_{4,n}$ and f are the amplitudes of the next-nearest-neighbour interactions; U is the on-site energy difference between the d_{xy} and $d_{xz,yz}$ orbitals, λ denotes the amplitude of SOC and m is the magnitude of the Zeeman interaction.

On the other hand, the interlayer hopping interaction is written as

$$t_{nm} \hat{d}_{n,ka\sigma}^\dagger \hat{d}_{m,kb\sigma} = \sum_{\mathbf{k}} [(\epsilon_{n,ka\sigma}^a \delta_{ab} \delta_{\sigma\sigma'} + f_{n,k}^{ab} \delta_{\sigma\sigma'}) \hat{d}_{n,ka\sigma}^\dagger \hat{d}_{m,kb\sigma}], \quad (9)$$

where

$$\begin{aligned} \epsilon_{n,ka\sigma}^{1=yz} &= -u_{1,n} - u_{2,n} \cos k_y, \\ \epsilon_{n,ka\sigma}^{2=xz} &= -u_{1,n} - u_{2,n} \cos k_x, \\ \epsilon_{n,ka\sigma}^{3=xy} &= -t_{2,n}, \\ f_{n,k}^{13} &= f_{n,k}^{s1} = 2if \sin k_x \\ f_{n,k}^{23} &= f_{n,k}^{s2} = 2if \sin k_y. \end{aligned} \quad (10)$$

Here we assume $n > m$ without losing generality; $u_{1,n}$ is the amplitude of the nearest-neighbour interaction and $u_{2,n}$ is the amplitude of the next-nearest-neighbour interaction. The parameters of the effective tight-binding Hamiltonian are summarized in Table 2.

QBC. The negative AHC under small magnetization in SRO can be explained by the $\mathbf{k} \cdot \mathbf{p}$ Hamiltonian expanded near QBCs. Neglecting rotation and tilting, a perovskite thin film has a square lattice structure. Without SOC, space group generators are four-fold rotation about the z axis (C_{4z}) and three mirrors M_x , M_y and M_z , where M_α changes the sign of the α coordinate. The $\mathbf{k} \cdot \mathbf{p}$ Hamiltonian valid near the Γ or M points is written as

$$H_{\text{QBC}} = E_0(\mathbf{k}) + \beta(k_x^2 - k_y^2)\tau_x + 2\beta k_x k_y \tau_y, \quad (11)$$

where $E_0(\mathbf{k})$ is part of the Hamiltonian proportional to identity and β is the coefficient of the $\mathbf{k} \cdot \mathbf{p}$ Hamiltonian.

$$(1, 0)^t = |d_{xz}\rangle + i|d_{yz}\rangle \equiv |+\rangle \text{ and } (0, 1)^t = |d_{xz}\rangle - i|d_{yz}\rangle \equiv |-\rangle$$

are the basis near the QBC. We now discuss the influence of SOC. The on-site SOC term is expressed as $\lambda \mathbf{L} \cdot \mathbf{S} = \lambda(L_x S_x + L_y S_y + L_z S_z)$, where \mathbf{S} is the spin operator. Since

$$\langle +1, \sigma | L_z S_z | +1, \sigma \rangle = -\langle -1, \sigma | L_z S_z | -1, \sigma \rangle = \lambda \sigma_z,$$

the effective Hamiltonian with SOC H is written as follows:

$$\begin{aligned} H &= H_{\text{QBC}} + H_{\text{SOC}} \\ &= E_0(\mathbf{k}) + \beta(k_x^2 - k_y^2)\tau_x + 2\beta k_x k_y \tau_y + \lambda \sigma_z \tau_z, \end{aligned} \quad (12)$$

where σ_z is +1 (-1) for majority (minority) bands. Thus the gap is opened and the relevant Berry curvature is given by

$$\Omega(\mathbf{k}) = \frac{\lambda \sigma_z}{\beta} \frac{2k^2}{(k^4 + \lambda^2/\beta^2)^{3/2}},$$

where the total Berry curvature $\int \Omega(\mathbf{k}) d\mathbf{k}$ is quantized to 2π . Unlike the Berry curvature induced by linear band crossing, which is maximum at $|\mathbf{k}|=0$, Berry curvature induced by QBC is zero at $|\mathbf{k}|=0$ and maximum at $|\mathbf{k}|=(2\lambda^2/\beta^2)^{1/4}$.

In SRO, although QBC formed by majority bands is closer to the Fermi level than that of minority bands, the former induces smaller Berry curvature. Since the bands at the M point are all hole-like, the Fermi level is between the majority bands for $k_1 < |\mathbf{k}| < k_2$ and minority bands for $k_1 + \Delta_1 < |\mathbf{k}| < k_2 + \Delta_2$ where Δ_1 and Δ_2 are positive numbers. Then, the Berry curvature that contributes to the AHE is

$$\int_{k_1}^{k_2} \Omega_{\text{maj}}(\mathbf{k}) d\mathbf{k} + \int_{k_1 + \Delta_1}^{k_2 + \Delta_2} \Omega_{\text{min}}(\mathbf{k}) d\mathbf{k} = \int_{k_1}^{k_1 + \Delta_1} \frac{\lambda}{\beta} \frac{2k^2}{(k^4 + \lambda^2/\beta^2)^{3/2}} - \int_{k_2}^{k_2 + \Delta_2} \frac{\lambda}{\beta} \frac{2k^2}{(k^4 + \lambda^2/\beta^2)^{3/2}}.$$

Here $\Omega_{\text{maj(min)}}(\mathbf{k})$ is the Berry curvature from the majority (minority) band. For small magnetization, Hall conductance can be negative, whereas for large magnetization, Berry curvature induced by minority bands becomes negligible and Hall conductance becomes positive.

The NL. Without SOC, the crossing between spin-up and spin-down bands form a NL. The corresponding Hamiltonian is written as

$$H_{\text{NL}} = \begin{pmatrix} E_\uparrow(\mathbf{k}) & 0 \\ 0 & E_\downarrow(\mathbf{k}) \end{pmatrix} = E_0(\mathbf{k}) + \Delta E(\mathbf{k})\sigma_z, \quad (13)$$

where $(1, 0)^t = |\psi_1(\mathbf{k}), \uparrow\rangle$, $(1, 0)^t = |\psi_2(\mathbf{k}), \downarrow\rangle$. Due to the SOC, spin U(1) symmetry is broken and the gap is opened. The SOC term is expressed as

$$\lambda(L_x S_x + L_y S_y + L_z S_z) = \frac{\lambda}{2}(L_+ S_- + L_- S_+) + \lambda L_z S_z, \quad (14)$$

$$\begin{aligned} \langle \psi_2(\mathbf{k}), \downarrow | L_+ S_- | \psi_1(\mathbf{k}), \uparrow \rangle &= \langle \psi_2(\mathbf{k}) | L_+ | \psi_1(\mathbf{k}) \rangle \\ &= \langle \psi_1(\mathbf{k}), \uparrow | L_- S_+ | \psi_2(\mathbf{k}), \downarrow \rangle^* = \langle \psi_1(\mathbf{k}) | L_- | \psi_2(\mathbf{k}) \rangle^* \\ &= \frac{\lambda}{2} [\alpha(\mathbf{k}) + i\beta(\mathbf{k})]. \end{aligned} \quad (15)$$

$$\therefore H_{\text{SOC}} = \alpha(\mathbf{k})\sigma_x + \beta(\mathbf{k})\sigma_y \quad (16)$$

Thus, the total Hamiltonian

$$H = H_{\text{NL}} + H_{\text{SOC}} = E_0(\mathbf{k}) + \Delta E(\mathbf{k})\sigma_z + \alpha(\mathbf{k})\sigma_x + \beta(\mathbf{k})\sigma_y.$$

If the Fermi energy lies between two energy bands, the Berry curvature is given by

$$\Omega(\mathbf{k}) = \frac{i \langle - | \partial H / (\partial k_x) | + \rangle \langle + | \partial H / (\partial k_y) | - \rangle + \text{c.c.}}{(\epsilon_- - \epsilon_+)^2}, \quad (17)$$

where $|+\rangle$ ($|-\rangle$) is a higher (lower) energy state, ϵ_+ (ϵ_-) is its energy eigenvalue, and c.c. represents complex conjugation. Similar to the calculation for QBC, the total Berry curvature is quantized to $\pm 2\pi$.

Let us note, however, that some NLs are intact under SOC. This is due to $M_z: z \rightarrow -z$ symmetry, which is local in both real and momentum space in two dimensions: $M_z |d_{xy}\rangle = |d_{xy}\rangle$, $M_z |d_{xz,yz}\rangle = -|d_{xz,yz}\rangle$, represented as

$$M_z = \begin{pmatrix} -1 & 0 & 0 \\ 0 & -1 & 0 \\ 0 & 0 & 1 \end{pmatrix} \otimes i\sigma_z.$$

Two bands with different mirror eigenvalues do not hybridize.

Relationship between OAM and Berry curvature. Here, we explain that OAM and Berry curvature show similar distributions. For simplicity, let us consider a two-band $\mathbf{k} \cdot \mathbf{p}$ Hamiltonian where the gap is opened by the SOC.

The Hamiltonian is written as

$$H = E_0(\mathbf{k}) + \beta(k_x^2 - k_y^2)\tau_x + 2\beta k_x k_y \tau_y + \lambda \sigma_z \tau_z, \quad (18)$$

where $\sigma_z = \pm 1$, which represents the direction of spin polarization. The energy spectrum is given as $E = E_0 \pm \sqrt{\lambda^2 + \beta^2 k^4}$ where the gap due to the SOC is proportional to λ .

The Berry curvature $\Omega(\mathbf{k})$ of the occupied band is

$$\Omega(\mathbf{k}) = 2\lambda \frac{\beta^2 k^2}{(\lambda^2 + \beta^2 k^4)^{3/2}} \sigma_z. \quad (19)$$

On the other hand, the z component of the OAM of the occupied band $|\text{occ}\rangle$ is defined as $\langle L_z \rangle = \langle \text{occ} | \tau_z | \text{occ} \rangle$, where

$$L_z(\mathbf{k}) = 2\lambda \frac{\lambda + \sqrt{\lambda^2 + \beta^2 k^4}}{(\lambda + \sqrt{\lambda^2 + \beta^2 k^4})^2 + \beta^2 k^4} \sigma_z. \quad (20)$$

The Berry curvature and OAM show a similar tendency since both of them are induced by the SOC that opens the gap at QBC. In particular, we note that the Berry curvature and OAM have the same sign, determined by λ .

Data availability

The data that support the findings of this study are available from the corresponding authors on request.

References

43. Kresse, G. & Furthmüller, J. Efficient iterative schemes for *ab initio* total-energy calculations using a plane-wave basis set. *Phys. Rev. B* **54**, 11169 (1996).
44. Perdew, J. P., Burke, K. & Ernzerhof, M. Generalized gradient approximation made simple. *Phys. Rev. Lett.* **77**, 3865–3868 (1996).
45. Blöchl, P. E. Projector augmented-wave method. *Phys. Rev. B* **50**, 17953–17979 (1994).
46. Pizzi, G. et al. Wannier90 as a community code: new features and applications. *J. Phys. Condens. Matter* **32**, 165902 (2020).
47. Liechtenstein, A. I., Anisimov, V. I. & Zaanen, J. Density-functional theory and strong interactions: orbital ordering in Mott-Hubbard insulators. *Phys. Rev. B* **52**, R5467–R5470 (1995).
48. Vaugier, L., Jiang, H. & Biermann, S. Hubbard U and Hund exchange J in transition metal oxides: screening versus localization trends from constrained random phase approximation. *Phys. Rev. B* **86**, 165105 (2012).
49. Bezdzicka, P., Wattiaux, A., Grenier, J., Pouchard, M. & Hagenmüller, P. Preparation and characterization of fully stoichiometric SrCoO_3 by electrochemical oxidation. *Z. Anorg. Allg. Chem.* **619**, 7–12 (1993).

Acknowledgements

We gratefully acknowledge discussions with J. R. Kim. This work is supported by IBS-R009-D1 and IBS-R009-G2 through the Institute for Basic Science (IBS) Center for Correlated Electron Systems. B.-J.Y. was supported by the Institute for Basic Science in Korea (grant no. IBS-R009-D1), Samsung Science and Technology Foundation under project no. SSTF-BA2002-06, the National Research Foundation of Korea (NRF) Grant funded by the Korea government (MSIT) (no. 2021R1A2C4002773, and no. NRF-2021R1A5A1032996). S.Y.P. was supported by the National Research Foundation of Korea (NRF) grant funded by the Korea government (MSIT) (no. 2021R1C1C1009494) and by the Basic Science Research Program through the National Research Foundation of Korea (NRF) funded by the Ministry of Education (no. 2021R1A6A1A03043957). The Advanced Light Source is supported by the Office of Basic Energy Sciences of the US Department of Energy under contract no. DE-AC02-05CH11231.

Author contributions

B.S., E.L., B.-J.Y. and C.K. conceived the project. S.Y.P., B.-J.Y. and C.K. led the project. B.S. synthesized and characterized the materials with support from B.K. and T.W.N.; B.S., W.K. and J.H. conducted ARPES measurements with support from J.D.D., J.S.O., J.K.J., D.O. and Y.K.; B.S., H.R. and S.H. conducted spin-resolved ARPES measurements. B.S. performed transport measurements. B.S. and B.K. performed magnetic measurements. M.K. and D.K. performed ionic liquid gating. B.S. analysed the experimental data. E.L. conducted tight-binding calculations and symmetry analysis. S.Y.P. conducted first-principles calculations. B.S., E.L., B.-J.Y. and C.K. wrote the paper with contributions from other authors. All authors participated in the discussions and commented on the manuscript.

Competing interests

The authors declare no competing interests.

Additional information

Supplementary information The online version contains supplementary material available at <https://doi.org/10.1038/s41563-021-01101-4>.

Correspondence and requests for materials should be addressed to Se Young Park, Bohm-Jung Yang or Changyoung Kim.

Peer review information *Nature Materials* thanks the anonymous reviewers for their contribution to the peer review of this work.

Reprints and permissions information is available at www.nature.com/reprints.